Optica Applicata, Vol. LIII, No. 4, 2023
DOI: 10.37190/oa230410

A refractive index sensor based on micro-nano fiber with chirped fiber Bragg grating embedded for a microfluidic chip

Zhanwu Xie[1,2], Haitao Yan[1,*], Pengfei Li[1]

[1]School of Electronic Engineering, Nanjing Xiao Zhuang University, Nanjing, China, 211171

[2]School of Computer and Electronic Information /School of Artificial Intelligence, Nanjing Normal University, Nanjing, China, 210023

[*]Corresponding author: yanhaitaoyht@163.com

A refractive index (RI) sensor based on micro-nano fiber (MN-fiber) with chirped fiber Bragg grating (CFBG) Fabry–Perot cavity (FP-cavity) for a microfluidic chip has been proposed. A single -mode fiber is drawn by hydrogen flame heading come into MN-fiber. Two CFBGs are written into this MN-fiber by the ultraviolet (UV) laser mask exposure method. One is at the tapered region, another is at the micro-nano region. Then a micro-nano fiber with chirped fiber Bragg grating (MN-CFBGs) FP-cavity sensor is formed. The Bragg reflection wavelengths of two CFBGs are 1620 nm, 3-dB bandwidth are above 50 nm. The reflectance of two CFBGs are 70% and 99%, respectively. The effects of reflectivity and bandwidth of the CFBGs FP-cavity, diameter and length of MN-fiber with this sensor's optical properties are analysed is and discussed. This sensor is embedded in a microfluidic chip and the MN-fiber region is immersion microfluid in different channels. The experimental results show that refractive index sensitivity of the sensor is –986 nm/refractive index unit (RIU), and the signal of the sensor has little noise. The CFBG-FP sensor not only has high sensitivity and lager measurement range, but also high contrast resonance signal and stability.

Keywords: micro-nano fiber, chirped fiber Bragg grating, Fabry–Perot cavity, microfluidic chip, sensor.

1. Introduction

In the past 20 years, optical fiber sensors have been widely studied because of their advantages such as low transmission loss, high sensitivity, easy integration and convenient distribution [1-4]. At present, distributed optical fiber sensors have been applied to engineering measurement. Fiber Bragg grating (FBG) is the most important optical passive device. And fiber sensor based on chirped fiber Bragg grating (CFBG) is a key part of fiber sensors [5]. Although the optical fiber sensors have been making a considerable progress, the development of information technology requires new op-

tical fiber sensors towards more miniaturization, integration, high sensitivity and high resolution [6]. At the same time, the application of fiber optical sensors for biochemical detection is a hot research topic recently [7]. Micro-nano fiber (MN-fiber) sensor has a microns size of the diameter, strong evanescent field [8], and large waveguide dispersion [9], which is widely used in detection, medical treatment, sensing, communication, *etc*. Compared with ordinary optical fiber sensor, the strong evanescent field property of MN-fiber can be realized in the light-wave coupling and information exchange with the external environment [10-13]. The MN-fiber sensor is the most effective optical fiber sensor to measure refractive index (RI).

Refractive index measurement and calibration are very important for biotechnology, drug screening, environmental monitoring and food detection [14, 15]. The RI optical fiber sensor has the highest sensitivity among the surface plasmon methods [16], which can reach 10^3 nm/RIU and even higher, such as a surface plasmon sensor achieving a high sensitivity of 4365.5 nm/RIU and a FoM of 51.61 RIU^{-1} [17]. However, this method needs fabrication of metal film which is a costly and is a complex process. Microfluidic chip is a hot field in the development of miniaturized total analysis systems. The measurement of RI is one of the important technologies in microfluidic chip detection technology. Many researchers had significant achievements, such as: a high sensitivity pH sensing by using a ring resonator, and also laser integrated into a microfluidic chip has been proposed [18]. A partially gold-coated TFBG is used as a microfluidic flow direction and rate vector sensor [19]. Bent waveguide structures because of low-cost, rapid chemical and biomedical sensing have been proposed, which are employing optofluidic RI sensors [20]. Moreover, an optofluidic RI sensor based on partial refraction has been reported [21]. And a RI sensor using microfiber-based Mach–Zehnder interferometer has been researched, which obtained sensitivity of about 7159 nm/RIU, achieved at a microfiber diameter of 2.0 μm [22].

As described above, the MN-fiber sensor is the most effective RI measurement sensor. However, when this MN-fiber is applied in the channel of microfluidic chip, it will be affected by the pressure and swift current of microfluidic, so it is difficult to obtain accurate measurement values. Thus, the MN-fiber RI sensor detection of microfluidic easily causes signal distortion. Moreover, after the mode interference is generated after the evanescent field leakage, the contrast of the interference fringe is relatively small, and it is easily disturbed by other signals of the external environment, resulting in signal instability.

In this paper, we had proposed an MN-fiber RI sensor with CFBG FP-cavity for the microfluidic chip. A MN-fiber was fabricated through the hydrogen gas flame heat drawing method, two CFBGs are written into this MN-fiber by the ultraviolet (UV) laser mask exposure method, one is at the tapered region, another is at the MN region. And then, CFBGs FP-cavity and MN-fiber come into being through organic fusion, and a new type of MN-CFBG FP-cavity RI sensor is formed. This MN-CFBG FP-cavity RI sensor can overcome the problem of microfluidic disturbance, energy attenuation and large signal noise, and the contrast of the interference fringes can be significantly increased by controlling the cone angle and length of the cone region. Since the CFBG

has lager bandwidth, so the CFBG-FP sensor not only has high sensitivity, but also increases measurement range.

2. Principle of sensor

Structure diagram of CFBG FP-cavity is shown in Fig. 1. The CFBG grating region length is L_1 and L_2, corresponding to CFBG1 and CFBG2 and the spacing between two CFBGs is L_3. The light waves are interfering in this CFBG-FP cavity. The Bragg wavelength along the grid axial direction of CFBG can be expressed as follows:

$$\lambda_z = 2n_{\text{eff}}(\Lambda_0 + Cz), \quad 0 \le z \le L \tag{1}$$

where λ_z is the characteristic wavelength of CFBG, n_{eff} is the fiber effective RI of the mode, Λ_0 is the grating initial period, C is the chirped rate, and z is the position of the CFBG axis upward. The period of the linear CFBG changes linearly along the grating length L. The CFBG is RI periodic distribution into the MN-fiber. The propagation constant in the fiber β is expressed as follows:

$$\beta = 2\pi n_{\text{eff}}/\lambda \tag{2}$$

Because the two CFBGs are in the conical region and MN-fiber region of MN-fiber, so the two CFBGs have different effective RIs when the light is incident to the first CFBG (the reflectance is 70%), and light will propagate into the MN-fiber and will be reflected by the second CFBG (the reflectance is 99%). Low reflectivity at one end and high reflectivity at the other end are more conducive to the signal output of the resonator, and reduce the insertion loss of the FP-cavity to ensure a higher spectral quality.

Meanwhile, high reflectivity is located in the transmission region of MN-fiber, which can fully contact the microfluidic and stabilize the transmission spectrum. When the light incidences the CFBGs FP-cavity, since the MN-fiber has the evanescent field, the light will be not only resonanced in the CFBGs FP-cavity, but also coupled with fluid of different RIs liquid around the MN-fiber.

According to the multi-beam propagation theory of FP-cavity, the interference between the MN-fiber mode and evanescent field models satisfies phase matching condition, which can be expressed as

$$\beta_1 L_1 - \beta_2 L_2 = \beta_3 L_3 = 2k\pi \tag{3}$$

where β_1, β_2, β_3 are the propagation constants of the first CFBG, the second CFBG and the MN-fiber between the two CFBGs, respectively. As shown in Fig. 1, L_1, L_2

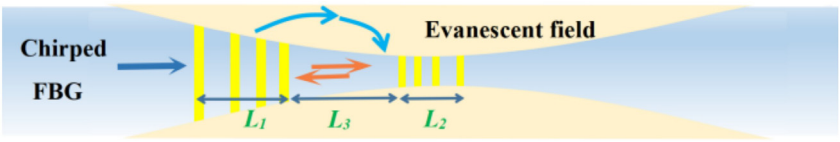

Fig. 1. The diagram of MN-FBG FP-cavity.

and L_3 are the optical paths of first CFBG, second CFBG and the MN-fiber between the two CFBGs, respectively. Only a certain beam with a certain oscillation frequency and a certain spatial distribution within the resonant bandwidth can cause sympathetic vibration in the cavity. When the RI of external fluid n is changed, the resonant wavelength of this sensor will be changed accordingly. So the variation of resonant wavelength with fluid RI can be measured and obtained, and this FP-cavity will greatly increase the light utilization efficiency and sensitivity, and the reflection coefficient of CFBGs will determine the intensity of output light.

3. Sensor fabrication

Firstly, a MN-fiber was fabricated by the hydrogen flame heading method. The preparation device diagram is shown in Fig. 2(a). An optical fiber (Corning SMF-28e) is fixed in a fixture on the displacement platform to ensure no bending under small stress, and the optical fiber in the heating region is suspended. The MN-fiber is composed of the transition zone and the waist zone. When the fiber is stretched, the volume is coserved:

$$\pi(r_{\mathrm{w}} + \delta r_{\mathrm{w}})^2(L + \delta x) = \pi r_{\mathrm{w}}^2 L \tag{4}$$

where the waist zone radius is r_{w}, the waist zone length is L, and the transition zone radius decreases with the fiber diameter, δr_{w} is a change in the radius and δx is a change in the length after the fiber is stretched [23]. From Eq. (4), we can find the function relationship between the radius of the waist area and the stretch length:

$$\frac{\mathrm{d}r_{\mathrm{w}}}{\mathrm{d}x} = -\frac{r_{\mathrm{w}}}{2L} \tag{5}$$

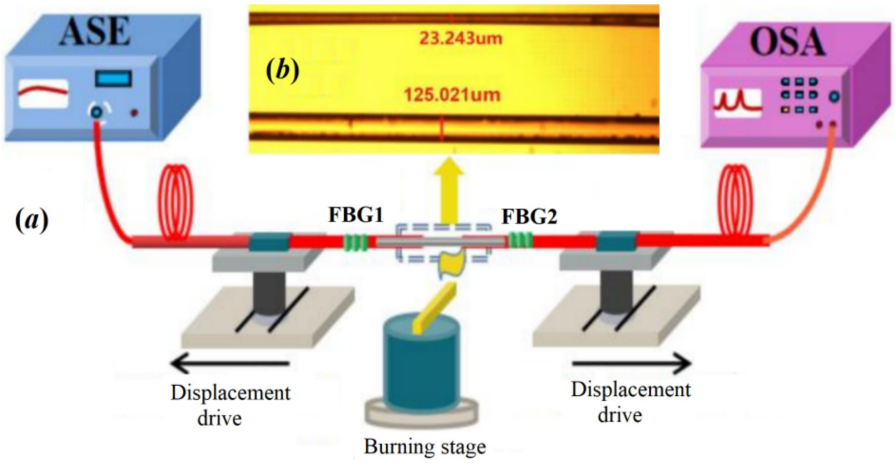

Fig. 2. Schematic diagram of MN-fiber preparation with real time monitoring. (a) Hydrogen flame heating to prepare MN-fiber, (b) microscope of MN-fiber and SMF-28e fiber.

Considering the strength of the evanescent field and the toughness of the MN-fiber, the process of fabricating the MN-fiber is as follows. The control platform model is Newport-Q8, hydrogen flow rate is 30 mL/min, two-ways motion at the same speed is 0.5 mm/s and pull length is about 80 mm. Since much larger hydrogen flame will cause the optical fiber to be disturbed and has an influence on the performance of fiber, small hydrogen flow and pull speed ensure MN-fiber is smooth and tapered area is longer. During the fabrication process, the spectra of this structure were real time monitored by supercontinuum sources (SuperK, FIU-15) and optical spectrum analyzer (OSA, AQ6370D).

After the above operation, the MN-fiber was natural cooling to room temperature, and a microscope (OPTEC, BDS200-PH) was used to observe the morphology of the MN-fiber. As shown in Fig. 2(b), the MN-fiber has a diameter of 23.243 μm, about 17.8% of the normal diameter, and the MN-fiber has smooth surface, good symmetry and transition from conical to cylindrical. The transition length of MN-fiber is about 40 mm and the length of the tapered area is about 20 mm.

Secondly, we fabricated two CFBGs on the MN-fiber by the UV mask exposure method. The fabricated process is described as follows. This MN-fiber was placed in hydrogen carrying equipment (ASP100-H2-T) with 60°C temperature for 7 days to form hydrogenated silicon in the fiber core. The operation sequence is to place this fiber, create a vacuum, fill with hydrogen to a pressure of 8 MPa, check the air tightness and set the hydrogen carrying parameters. And then, two CFBGs were written by using 248 nm UV exciter laser (MLI-500LC) and chirped phase mask. The phase mask with a period of 1119.56 nm, length of 10 cm and chirp rate 18.5 nm/cm was selected. In order to accurately match the parameters of two CFBGs, we applied prestress of 0.3 N to ensure that the fiber was in tensile state after selecting the appropriate initial position. The same exposure Hamming function, output voltage (600 V) and energy (6.23 mJ) of laser were used in the process. Then, two CFBGs with the different parameters (grating length is 20 mm, exposure time is 45 and 100 s) were written in the MN-fiber at the cylindrical region and tapered region; the reflectance is 70% and 99% for the first CFBG and second CFBG. In order to remove the effect of hydrogen molecules on wavelength and keep the performance of CFBG stable, this fiber was at 150°C temperature about 12 hours.

Finally, we obtained CFBGs FP-cavity structure into the MN-fiber. To compare the spectral effect of the CFBG FP-cavity, we also made the single CFBG on an ordinary fiber. The transmission spectra of a CFBG and the MN-CFBG FP-cavity at the 25°C are shown in Fig. 3. The red lines are the spectrum of CFBG and the blue lines are the spectrum of MN-CFBG FP-cavity.

Compared with the initial spectra of a single CFBG, which could be seen in Fig. 3, the resonance peaks were significantly existing from 1590 to 1650 nm, as we expected. The center wavelength was about 1620 nm, and the 3-dB bandwidth was above 50 nm. Because the strength of the resonance is affected by the evanescent field at the tapered region, the intensity decreases significantly 1590–1610 nm and 1642–1650 nm. The profile of the resonance peak is consistent with the spectrum of a single CFBG at

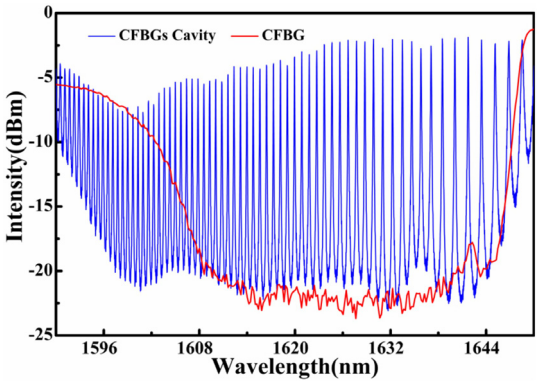

Fig. 3. Transmission spectra of a CFBG and MN-CFBG FP-cavity.

the 1610–1642 nm. However, the periodicity of this resonance spectrum is not consistent. At the long wave position, the period of optical signal resonance is larger. The principal reason for this phenomenon is that the CFBG has chirp rate, and the distance of grating grid between each corresponding wavelength is different. In other words, the length of CFBGs FP-cavity is different for different wavelengths. Therefore, it is different from ordinary multi-beam interference, and the period of spectral resonance is different. Richer spectra information of this CFBGs FP-cavity will greatly improve the wavelength resolution, stability and measuring range. The spectra result shows the feasibility and reliability of the above preparation methods and the sensor.

4. Experimental measurements and discussion

These sensors were embedded in a microfluidic chip and the MN-fiber region was immersed in channels with different microfluids at room temperature 25°C. The pump and chip in this experiment were provided by Tianjin Micro-Nano Chip Technology Co. Ltd., the channel is cylindrical with a diameter of 50 μm. We fixed one end of the MN-fiber with AB glue at the bottom of corresponding channel, and then, we applied prestress of 0.04 N to ensure that the MN-fiber sensor was in a tensile state; the other end of this sensor was fixed later. This prestress brought to this sensor can effectively overcome the instability and noise caused by the viscosity effect, resistance factor and turbulence of microfluidic. And then, an experiment was designed to measure the RI sensing for microfluidic chip by this MN-CFBGs FP-cavity sensor. Some different concentrations of the pure glycerinum with pure water are configured as microfluid to be measured. Continuous ambient RI was varying from 1.3330 to 1.3350 with the step of around 0.0005 [24]. We used smaller RI range changes in order to better verify the stability and sensitivity of this sensor. The measurement structure diagram and physical photo are shown in Fig. 4.

The different microfluid was driven by a micro flow pump (LSP01-3A) into the channels, and the injection flow rate is 0.012 μL/min. The sensors are connected super-

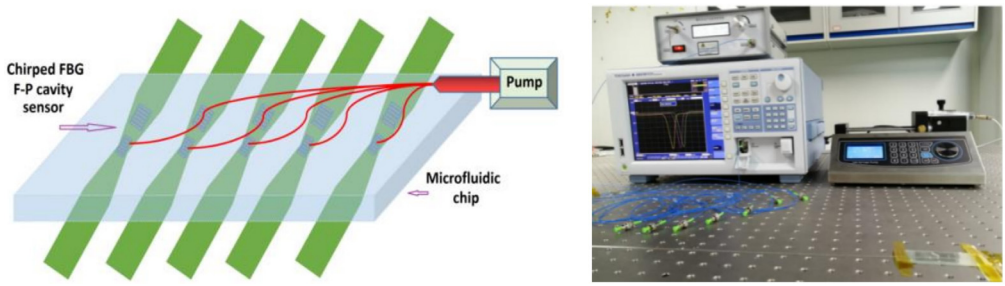

Fig. 4. The diagram of sensor embedded microfluidic chip and physical photo of sensor measurement.

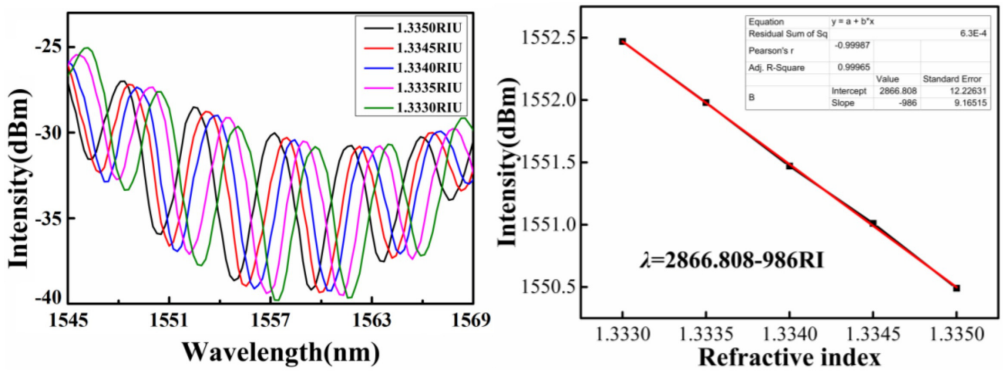

Fig. 5. Spectra of sensors with different concentrations of microfluidic different channels of microfluidic chip and linear fitting.

continuum sources and OSA similar to Fig. 2, an optical beam splitter is added to connect sensors of multiple channels. And then, the spectra of sensors were recorded by OSA and shown in Fig. 5.

Since the different RI microfluids caused the effective RI of the MN-fiber changed the effective optical path of the CFBGs FP-cavity will be also changed, and these will lead to changes in the resonant wavelength. It can be seen from Fig. 5 that the resonance wavelength keeps blue-shifted with the increase of the fluidic RI. According to Eq. (3), external liquid RI increase will lead to the propagation coefficient β_2 increased, so that the resonance peak of the wavelength will also increase in order to satisfy the resonance condition. The experimental results agree with the theoretical analysis. The spectra are very smooth and almost noisless, and the contrast of the interference fringes of the spectra is 0.114 at 1550 nm, which indicates that the signal noise of the MN-CFBGs FP-cavity sensor is very small in different environments and obviously improved. At the same time, the intensity of transmitted light increases slightly with the increase of the RI due to evanescent field coupling efficiency enhancement by FP-cavity, and the loss of the transmission spectra is reduced with the RI increased. Define the sensitivity of the sensor $S = \Delta\lambda/\Delta\text{RI}$, the sensor sensitivity is about –986 nm/RIU. Besides the sensor sensitivity, the figure of merit (FoM) is another widely used parameter that

describes the sensing performance of an optical sensor [25,26]. The FoM is defined as FoM = Sensitivity/FWHM, where FWHM is the full width at half maximum. FWHM of the resonance peak is about 1.8 nm, so the FoM of this RI sensor is about 547.8 RIU^{-1}.

In addition, we selected one period at 1550–1553 nm position to analyze the sensor properties. Linear fitting is carried out between RI change and wavelength drift. The linear fitting results are shown in Fig. 5. The linearity is 0.99965, and the minimum resolution wavelength of OSA is $\lambda_{min} = 0.02$ nm, so we can obtain the resolution $R = \lambda_{min}/S = 0.00002$ RIU.

5. Conclusion

In summary, a microfluidic RI sensor for microfluidic chip based on MN-CFBGs FP-cavity structure has been proposed and demonstrated, and fabrication method of this sensor has been described in detail. We designed the experiment to measure this sensor in a microfluidic chip and to obtain experimental results. The resonant wavelength of our sensor is the blue-shift with the increase in the RI of the external environment. The RI sensitivity is –986 nm/RIU and the FoM of this RI sensor is about 547.8 RIU^{-1}, and its linearity between RI changes and resonant wavelength drift is 0.99965. Moreover, the contrast of the interference fringes of the sensor is 0.114. The FP-cavity consists of high and low reflectivity of CFBG with lager bandwidth. The optical spectrum quality of the sensor is obviously increased and the dynamic response range is also significantly increased. If our sensor has longer cavity length and wider CFBG bandwidth, this sensor can have even higher sensitivity, resolution and lager measuring range. In addition, when we are placing this sensor to higher RI microfluid, we know “peak value” light power is rising instead of falling. Because of the advantages of small size, low noise and low power loss, this sensor is very suitable for the detection of microfluidic chips.

Funding
This work was sponsored by NSFC programs No. 61675064 and No. 51875292.

Disclosures
The authors declare no conflicts of interest.

Acknowledgements
This work was completed with the support of professional equipment from Puyang Photoelectric Industry Technology Research Institute.

Data availability
Data underlying the results presented in this paper are not publicly available at this time but may be obtained from the authors upon reasonable request.

References

[1] Takahashi N., Yoshimura K., Takahashi S., Imamura K., *Development of an optical fiber hydrophone with fiber Bragg grating*, Ultrasonics **38**(1-8), 2000: 581-585. https://doi.org/10.1016/S0041-624X(99)00105-5

[2] Jiang L., Yang J., Wang S., Li B., Wang M., *Fiber Mach-Zehnder interferometer based on micro-cavities for high-temperature sensing with high sensitivity*, Optics Letters **36**(19), 2011: 3753-3755. https://doi.org/10.1364/OL.36.003753

[3] Vargas-Rodriguez E., Guzman-Chavez A.D., Baeza-Serrato R., Garcia-Ramirez M.A., *Optical fiber FP sensor for simultaneous measurement of refractive index and temperature based on the empirical mode decomposition algorithm*, Sensors (Basel) **20**(3), 2020: 664. https://doi.org/10.3390/s20030664

[4] Yilmaz G., Karlik S.E., *A distributed optical fiber sensor for temperature detection in power cables*, Sensors and Actuators A **125**(2), 2006: 148-155. https://doi.org/10.1016/j.sna.2005.06.024

[5] Xie Z., Yan H., Zhang H., Zhao X., Han D., *Cantilever deflection optical fiber sensor based on a chirped fiber grating Fabry-Perot cavity*, Applied Optics **60**(27), 2021: 8384-8389. https://doi.org/10.1364/AO.434672

[6] Ma G.M., Zhou H.Y., Zhang M., Li C.R., Yin Y., Wu Y.Y., *A high sensitivity optical fiber sensor for GIS partial discharge detection*, IEEE Sensors Journal **19**(20), 2019: 9235-9243. https://doi.org/10.1109/JSEN.2019.2925848

[7] Cennamo N., Zeni L., *Polymer optical fibers for sensing*, Macromolecular Symposia **389**(1), 2020: 1900074. https://doi.org/10.1002/masy.201900074

[8] Jiang X., Tong L., Vienne G., Guo X., Tsao A., Yang Q., Yang D., *Demonstration of optical microfiber knot resonators*, Applied Physics Letters **88**(22), 2006: 223501. https://doi.org/10.1063/1.2207986

[9] Samavati Z., Samavati A., Ismail A.F., Othman M.H.D., Rahman M.A., *Comprehensive investigation of evanescent wave optical fiber refractive index sensor coated with ZnO nanoparticles*, Optical Fiber Technology **52**, 2019: 101976. https://doi.org/10.1016/j.yofte.2019.101976

[10] Zhang L., Lou J., Tong L., *Micro/nanofiber optical sensors*, Photonic Sensors **1**(1), 2011: 31-42. https://doi.org/10.1007/s13320-010-0022-z

[11] Stern L., Desiatov B., Goykhman I., Levy U., *Nanoscale light-matter interactions in atomic cladding waveguides*, Nature Communications **4**, 2013: 1548. https://doi.org/10.1038/ncomms2554

[12] Qi Y., Zhang J., Feng Q., Zhang X., Liu Y., Han Y., *A novel high sensitivity refractive index sensor based on multi-core micro/nano fiber*, Photonic Sensors **9**(3), 2019: 197-204. https://doi.org/10.1007/s13320-019-0554-9

[13] Cai L., Pan J., Zhao Y., Wang J., Xiao S., *Whispering gallery mode optical microresonators: Structures and sensing applications*, physica status solidi (a) **217**(6), 2020: 1900825. https://doi.org/10.1002/pssa.201900825

[14] Zhang J., Sun Q., Liang R., Jia W., Li X., Wo J., Liu D., Shum P.P., *Microfiber Fabry–Perot interferometer for dual-parameter sensing*, Journal of Lightwave Technology **31**(10), 2013: 1608-1615. https://doi.org/10.1109/JLT.2013.2252145

[15] Bag S.K., Wan M., Sinha R.K., Varshney S.K., *Design and characterization of surface relief grating on etched multimode optical fiber for refractive index sensing*, Sensors and Actuators A **303**, 2020: 111836. https://doi.org/10.1016/j.sna.2020.111836

[16] Yan H.T., Liu Q., Ming Y., Luo W., Chen Y., Lu Y.Q., *Metallic grating on a D-shaped fiber for refractive index sensing*, IEEE Photonics Journal **5**(5), 2013: 4800706. https://doi.org/10.1109/JPHOT.2013.2284244

[17] Liu Y., Peng W., *Fiber-optic surface plasmon resonance sensors and biochemical applications: A review*, Journal of Lightwave Technology **39**(12), 2021: 3781-3791. https://doi.org/10.1109/JLT.2020.3045068

[18] LI D.Y., ZHANG H., LI Z., ZHOU L.W., ZHANG M.D., PU X.Y., SUN Y.Z., LIU H., ZHANG Y.X., *High sensitivity pH sensing by using a ring resonator laser integrated into a microfluidic chip*, Optics Express **30**(3), 2022: 4106-4116. https://doi.org/10.1364/OE.449943

[19] SHEN C., LIU D., LIAN X., LANG T., ZHAO C., SEMENOVA Y., ALBERT J., *Microfluidic flow direction and rate vector sensor based on a partially gold-coated TFBG*, Optics Letters **45**(10), 2020: 2776-2779. https://doi.org/10.1364/OL.392511

[20] LIU I.C., CHEN P.C., CHAU L.K., CHANG G.E., *Optofluidic refractive-index sensors employing bent waveguide structures for low-cost, rapid chemical and biomedical sensing*, Optics Express **26**(1), 2018: 273-283. https://doi.org/10.1364/OE.26.000273

[21] SEOW Y.C., LIM S.P., KHOO B.C., LEE H.P., *An optofluidic refractive index sensor based on partial refraction*, Sensors and Actuators B **147**(2), 2010: 607-611. https://doi.org/10.1016/j.snb.2010.03.076

[22] WO J., WANG G., CUI Y., SUN Q., LIANG R., SHUM P.P., LIU D., *Refractive index sensor using microfiber-based Mach-Zehnder interferometer*, Optics Letters **37**(1), 2012: 67-69. https://doi.org/10.1364/OL.37.000067

[23] LI P., YAN H., XIE Z., ZHAO X., HAN D., *A bandwidth response humidity sensor with micro-nano fibre Bragg grating*, Optical Fiber Technology **53**, 2019: 101998. https://doi.org/10.1016/j.yofte.2019.101998

[24] LI J., SHEN X., SUN L.P., GUAN B.O., *Characteristics of microfiber Fabry-Perot resonators fabricated by UV exposure*, Optics Express **21**(10), 2013: 12111-12121. https://doi.org/10.1364/OE.21.012111

[25] XU Y., WU L., ANG L.K., *Surface exciton polaritons: A promising mechanism for refractive-index sensing*, Physical Review Applied **12**, 2019: 024029. https://doi.org/10.1103/PhysRevApplied.12.024029

[26] ALBERT J., SHAO L.Y., CAUCHETEUR C., *Tilted fiber Bragg grating sensors*, Laser & Photonics Reviews **7**(1), 2013: 83-108. https://doi.org/10.1002/lpor.201100039

Received January 29, 2023
in revised form March 29, 2023